


Bisrat Wolde*
Lee F. Mortimer
Michael Fairweather

Stokes Number Effects on Deposition in Particle-Laden Turbulent Pipe Flows

The ability to predict particle dispersion, interaction, and deposition in turbulent pipes is of value in improving the transport and process efficiency of high concentration particulate flows. In this work, the settling and deposition behavior of suspensions of dense particles in a cylindrical pipe has been studied using direct numerical simulation coupled with Lagrangian particle tracking, with the influence of Stokes number on deposition behavior examined. From the analysis performed, it can be concluded that particle deposition is sensitive to Stokes number. In particular, the dispersion function and mean vertical displacement of the particles are demonstrated to decrease considerably faster with time at the higher Stokes number. Particle migration towards the lower wall regions of the pipe also shows the formation of a solid bed of these particles, whilst over the same time period only dune-like structures are produced at the lower Stokes number. Further analysis of the particle dynamics confirms these findings and generates insight into the particle dynamics within the deposition regions.

 This is an open access article under the terms of the Creative Commons Attribution License, which permits use, distribution and reproduction in any medium, provided the original work is properly cited.

Keywords: Direct numerical simulation, Lagrangian particle tracking, Particle deposition, Stokes number

Received: December 15, 2022; *revised:* February 24, 2023; *accepted:* April 17, 2023

DOI: 10.1002/ceat.202200606

1 Introduction

Accurate simulation of multiphase turbulent flows is of fundamental importance in many industrial and scientific research applications. Additionally, the generation of understanding through accurate modeling of turbulent multiphase flows is valuable across numerous industries such as chemical engineering, agriculture, and nuclear waste processing [1]. Very few direct numerical simulation (DNS) studies have been performed in the past to investigate turbulent pipe flows at moderately high Reynolds numbers ($Re_b = 11\,700$), and even fewer including the presence of a particulate phase. In the past, multiphase DNS investigations have generally been performed including only one-way coupling between the particles and the fluid, and at low Reynolds numbers [2].

Many researchers have conducted numerical simulations of fluid flow in cylindrical geometries, with notable works utilizing direct numerical simulation (DNS) including Fatica and Orlandi [3], Wagner et al. [4], and Fukagata and Kasagi [5]. Although these works improved our understanding of such flows, they were simulated at low Reynolds number. For example, Wagner et al. [4] used a pipe length of $L = 10R$ and shear Reynolds number of $Re_\tau \cong 320$. El Khoury et al. [6] subsequently applied a high-order spectral element method to predict flows at four different shear Reynolds numbers, based on radius, of $Re_\tau \cong 180, 360, 550$, and 1000 in a smooth pipe with a characteristic length $L \cong 25R$. Experimental studies of single-phase flow in pipes are numerous, but the settling and deposition behavior of suspensions of dense particles was examined

by Tsuji et al. [7] using laser Doppler velocimetry, and by Rice [8] employing acoustic Doppler velocimetry which established the critical deposition velocity of particles through experiments that investigated their resuspension from a particle bed [8].

There is, however, a noticeable absence of four-way coupled (i.e., both particle-fluid and particle-particle interactions are taken into account) DNS-based simulations of particle-laden flows, particularly in cylindrical geometries. Further, no previous modeling studies have considered the onset of particle deposition in such flows. As computational power increases it is now possible to perform such fully coupled simulations. The effects of particles on the fluid and interparticle collisions in turbulent pipe flows at moderately high Reynolds numbers are therefore investigated here, with the emphasis placed on analysis of the results to determine particle dispersion and particle deposition out of the flow to form solid beds or dune-like structures.

In this work, a predictive methodology was developed based on DNS coupled with Lagrangian particle tracking (LPT) to study the details of particle deposition at two different particle Stokes numbers based on shear units, $Sf^+ = 5.55$ and 16.78. An openly available computational fluid dynamic solver, Nek5000,

Bisrat Wolde (pmbw@leeds.ac.uk), Dr. Lee F. Mortimer, Prof. Michael Fairweather

School of Chemical and Process Engineering, Faculty of Engineering and Physical Sciences, University of Leeds, Leeds, LS2 9JT, United Kingdom.

has been utilized as the basis for the work reported [9]. The DNS code has been further extended with a four-way coupled LPT code to allow for high-fidelity simulation of depositing particle-laden pipe flows.

2 Methodology

2.1 Single-Phase Flow Simulations

To solve the descriptive fluid flow equations, the DNS solver Nek5000 was used, as developed by Fischer et al. [9]. This solver is based on the spectral element method, an efficient parallelizable, high-order weighted residual technique with excellent accuracy and low numerical dispersion and dissipation [10]. The Navier-Stokes equations are solved in non-dimensional form. In this work, all simulations were performed under the assumption that the fluid was Newtonian. The system studied was a pressure-driven incompressible turbulent flow in a long straight pipe with circular cross section and an internal diameter D . The time-dependent non-dimensional Navier-Stokes equations are given as:

$$\nabla \cdot \underline{u}^* = 0 \quad (1)$$

$$\frac{\partial \underline{u}^*}{\partial t^*} + (\underline{u}^* \cdot \nabla) \underline{u}^* = -\nabla p^* + \frac{1}{Re_b} \nabla \cdot \underline{\tau}^* + f_i \quad (2)$$

Here, $\underline{u}^*(\underline{x}^*, t^*)$ is the fluid velocity vector, non-dimensionalized using the bulk velocity U_b , with the position vector, \underline{x}^* , and time, t^* , non-dimensionalized as $\underline{x}^* = \underline{x}/D$ and $t^* = tU_b/D$, respectively. The term p^* is the non-dimensionalized pressure for high-velocity flow, $p^* = p/\rho U_b^2$. The bulk Reynolds number, Re_b , is defined as $Re_b = U_b D/\nu$, where ν is the fluid kinematic viscosity. Finally, $\underline{\tau}^*$ is the non-dimensionalized fluid stress tensor, $\underline{\tau}^* = \nabla \underline{u}^* + \nabla \underline{u}^{*T}$, and f_i is a forcing term representing the driving pressure gradient and the two-way interaction between the fluid and the particles, detailed later.

Eqs. (1) and (2) are solved numerically using the spectral element method along with appropriate boundary conditions. In three-dimensional space, these equations are discretized as grid points by the Lagrange-Galerkin approximation method. N^{th} -order Lagrange polynomial interpolants on Gauss-Lobatto-Legendre (GLL) points are implemented as a basis for velocity space and Lagrangian interpolants of order $N-2$ on Gauss-Legendre quadrature points are employed for pressure space. Resolution of the Kolmogorov length scale was confirmed.

The computational domain consisted of a circular pipe of diameter D and length $L = 12.5D$, partitioned into 36 576 spectral elements. Within the macro-elements the velocity field was represented by high-order tensor-product GLL polynomial expansions of order N . The flow in the streamwise direction was forced by a constant pressure gradient. The shear Reynolds numbers based on the shear stress velocity considered below were $Re_\tau \approx 277$ and $Re_\tau \approx 720$. For both simulations, the same mesh topology and number of spectral elements was used. Gauss-Lobatto-Legendre quadrature points ($N = 7$) were used to distribute the vertices in each element [11]. The total num-

ber of elements and equivalent GLL grid points used are given in Tab. 1.

Table 1. Continuous phase mesh and system parameters.

Re_b	Re_τ	Elements	GLL grid points
3975	277	36 576	18 726 912
11 700	720	36 576	18 726 912

2.2 Lagrangian Particle Tracking

LPT solves a force-balance equation for each particle in the system, represented as an impenetrable computational sphere, under the assumption of point particles. The particle equations of motion for all forces considered in the multiphase flows are presented in Eqs. (3) and (4). In this research, a modified Maxey and Riley [12] equation was employed. The non-dimensional forms of the equations of motion for spherical particles, as implemented in the simulations, are:

$$\underline{u}_p^* = \frac{\partial \underline{x}_p^*}{\partial t^*} \quad (3)$$

$$\frac{\partial \underline{u}_p^*}{\partial t^*} = \frac{1}{M_{VM}} \times \left[\frac{3C_D |\underline{u}_s^*|}{4d_p^* \rho_p^*} \underline{u}_s^* + \frac{1}{Fr} \left(1 - \frac{1}{\rho_p^*} \right) \widehat{g}^* + \frac{3C_L}{4\rho_p^*} (\underline{u}_s^* \times \underline{\omega}_f^*) \right] + \left[\frac{D' \underline{u}_f^*}{2\rho_p^* Dt^*} + \frac{D \underline{u}_f^*}{\rho_p^* Dt^*} \right] \quad (4)$$

In Eqs. (3) and (4), \underline{u}_p^* is the particle velocity vector, \underline{x}_p^* is the particle position vector, C_D is the drag coefficient, and \underline{u}_s^* is the slip velocity given as $\underline{u}_f^* - \underline{u}_p^*$, where \underline{u}_f^* and \underline{u}_p^* are the fluid (spectrally interpolated at the position of the particle) and particle velocity vectors, respectively. Also, d_p^* is the particle diameter, ρ_p^* the density ratio, and Fr is the Froude number, which is defined as $Fr = u_b^2/gD$, where g is the gravitational acceleration and \widehat{g}^* is a unit vector in the direction of gravitational attraction. $\underline{\omega}_f^*$ is the vorticity of fluid which is given by $\underline{\omega}_f^* = \nabla \times \underline{u}_f^*$, and the full equation is divided by $M_{VM} = \left(1 + 1/2\rho_p^* \right)$ to account for the virtual mass force. The particle bulk Stokes number is given as $St_b = d_p^{2*} \rho_p^* Re_b/18$, and the shear Stokes number as $St^+ = d_p^{2*} \rho_p^* Re_\tau^*/18$. A detailed explanation of these forces is provided by Mortimer et al. [13].

The drag force occurs due to particle movement through a resistive fluid phase and is a dominant force in the fluid-particle flow [14], while the lift force arises due to shear across the particle. Saffman [15] studied the strength and direction of the lift force for low particle Reynolds number and later Dandy and Dwyer [16] extended this work to high particle Reynolds numbers. The virtual mass and pressure gradient forces were based on the fluid acceleration and local pressure gradient,

respectively [17]. A gravitational force was also applied in the vertical direction in all simulations. To account for two-way momentum coupling, for a given computational cell, the mean forces applied to each particle during a numerical timestep were also distributed to the local fluid cell, as applied in Eq. (2). The effect of the fluid on the particles and the particles on the fluid was considered through use of Eq. (5) which is introduced as an additional term in the Navier-Stokes equations:

$$f_{2w}^{*i} = \frac{1}{V_i^*} \sum_{i=1}^N \frac{\partial u_{pi}^*}{\partial t^*} \quad (5)$$

where v_i^* is the volume of the computational cell, and i is the number of particles used [13].

The simulations were also performed four-way coupled, accounting for collisions between particles. A deterministic, hard-sphere, elastic collision model was utilized. A deterministic grid-based binary collision search algorithm was also used to reduce computational cost. As the particles are rigid and undeformable, it is reasonable to assume that the particle collision contact time is shorter than the LPT time step, and it was ensured that particle collisions were not missed by reducing the time step such that the distance travelled by a particle in a single time step was less than the diameter of the particle. By comparing the relative collision velocities of the particles upon impact, the code can identify which have collided and calculate rebound velocities [18].

The Lagrangian particle tracker was developed to model large quantities of dispersed solids and runs concurrently with Nek5000. A fourth-order Runge-Kutta method was implemented to solve the particle equations of motion for each particle at every time-step. To initialize the computations, the particles were injected at random positions within the fully developed fluid flow domain and assigned the fluid velocity at that location. Particle collisions with the pipe wall were considered to be elastic. Periodic boundary conditions were applied at the extents of the streamwise direction and no-slip conditions at the wall at a radial distance $r^* = 0.5$. Statistical data was gathered for the fully coupled simulations after a few particle response times ($t^* = 20$) to allow time for the injected phase to adjust to the surrounding fluid flow.

2.3 Particle Deposition

Rice [8] investigated the settling and deposition behavior of suspensions of dense particles in closed cylindrical pipes using ultrasonic methods, with the onset of particle deposition and resuspension from beds studied. In the experiments performed, a range of parameters were considered, though pipe diameter was not. Two ways of evaluating the critical deposition velocity were proposed, i.e., the velocity at which particles first start to deposit out in a flow. Both particles depositing as the flow rate was decreased, and in contrast when the particles were resuspended from the pipe floor as the flow rate was increased, were considered, arguing that these approaches were equivalent and represented different ways to obtain the same critical deposition velocity. In the past, the critical deposition velocity was

determined by a visual observation of the flow's suspension [19], and scouring sand dune formation [20].

In the present study, depositing pipe flows were considered using the DNS and LPT codes at two different Stokes numbers, $St^* = 5.55$ and 16.78 . These were chosen to represent those considered in Rice's [8] resuspension, and Sinclair's [19] and Al-lababidi's [20] deposition, experimental datasets. For the present simulation, the lowest and the highest Stokes numbers have been selected from across that range. A fully developed particle-laden turbulent pipe flow at $Re_\tau = 720$ was first run, with the flow rate subsequently decreased regularly until particle deposition occurred. To achieve this, the pressure gradient along the pipe was gradually lowered by 2% every 2000 time steps ($t^* = 2$).

The bulk Stokes response times for $St^* = 5.55$ and 16.78 particles are 0.125 and 0.379, respectively. The time interval between pressure drops is therefore significantly greater than the response bulk Stokes number to ensure particles have enough time to suitably adjust to the modified flow. The dispersion function and mean displacement of the particles were also monitored, with the dispersion function, $D_{y(t)}^*$, defined as:

$$D_{y(t)}^* = \left(\sum_{i=1}^{N_p} \frac{(y_{i(t)}^* - y_{m(t)}^*)^2}{N_p} \right)^{1/2} \quad (6)$$

Here, $y_{i(t)}^*$ is the particle displacement in the vertical direction, $y_{m(t)}^*$ is the mean vertical particle position, sampled across the entire domain, and N_p denotes the total number of particles [21]. Tab.2 shows the configuration of the depositing pipe flows. In both cases, the same concentration, particle diameter, and number of particles were used. It should be noted that the maximum value of the volume fraction ϕ found in regions outside the deposition zone considered below was 2.5×10^{-3} .

Table 2. Particle phase parameters.

Parameter	Shear Reynolds number, $Re_\tau = 720$	
	$St^* = 5.55$	$St^* \cong 16.78$
Particle diameter, d_p^*	0.005	0.005
Axial length	12.5D	12.5D
Number of particles, N_p	105k	105k
Bulk Stokes number, St_b	0.125	0.379
Density ratio, ρ_p^*	7.71	23.3
Volume fraction, ϕ	0.0007	0.0007
Particle timestep, Δt^*	0.001	0.001

3 Results and Discussion

3.1 Single-Phase Flow Validation

Single-phase flow simulations were performed at shear Reynolds numbers of $Re_\tau = 277$ and $Re_\tau = 720$ in order to validate the DNS approach being used. In each simulation, statistical data were gathered for analysis. The simulation results were compared with various DNS and experimental datasets available in the literature at, or approximately equal to, the Reynolds numbers of the simulations performed. For each simulation the mean velocity profiles, root mean square of the velocity fluctuations, and shear stress, were compared. Only literature data with incompressible and Newtonian fluid flows was used for validation and, where possible, multiple experiments and DNS datasets were compared with the current simulations.

Fig. 1a shows the axial mean velocity profile of the present predictions at a shear Reynolds number $Re_\tau = 720$, and compares this with the DNS results of El Khoury et al. [6] at $Re_\tau = 720$ and Singh et al. [22] at $Re_\tau \approx 640$. The present work agrees with the results of El Khoury et al. [6] but slightly deviates when contrasted with those of Singh et al. [22], likely due to the difference in Reynolds number. The results are additionally compared with the den Toonder et al. [2] experimental dataset at $Re_\tau \approx 630$. These results correlate well with the present work given the difference in Reynolds number.

Fig. 1b displays the axial, z_{rms}^* , radial, r_{rms}^* , azimuthal, θ_{rms}^* , normal stress profiles, and the Reynolds shear stress, $\langle u_z u_r \rangle^*$, at $Re_\tau = 720$ showing good agreement with El Khoury et al. [6], Singh et al. [22], and den Toonder et al. [2]. On the pipe centerline, all the simulations and experimental data are in good agreement with the inner scaled profiles of the present DNS. Overall, comparison of the normal and shear stresses, as a function of $0.5 - r^*$, gives confidence in the present continuous phase predictions. Similar agreement with literature data was also found for the $Re_\tau = 277$ case considered.

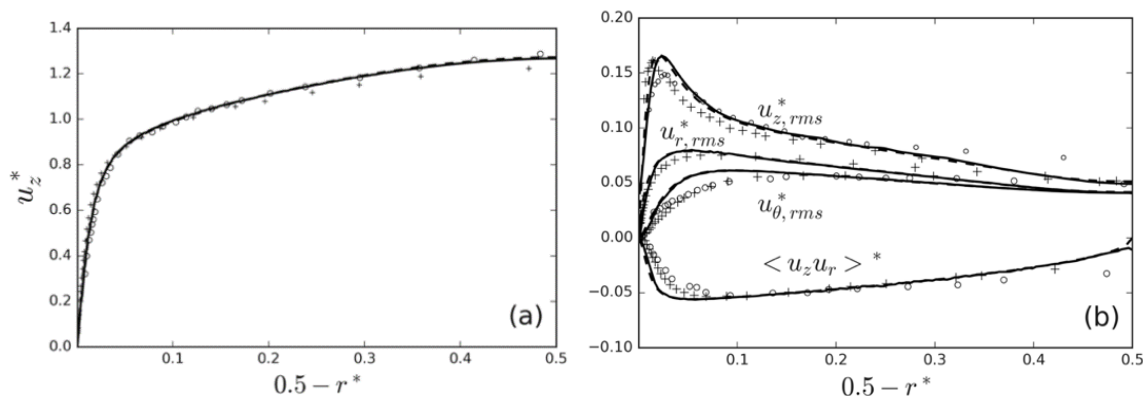


Figure 1. (a) Mean axial velocity u_z^* : — present DNS at $Re_\tau = 720$; - - El Khoury et al. (2013) DNS at $Re_\tau = 720$; + Singh et al. (2018) DNS at $Re_\tau \approx 640$; \circ den Toonder et al. (1997) measurements at $Re_\tau \approx 630$; (b) Axial, z_{rms}^* , radial, r_{rms}^* , and azimuthal, θ_{rms}^* , normal stresses and Reynolds shear stress, $\langle u_z u_r \rangle^*$: — present DNS at $Re_\tau = 720$; - - El Khoury et al. (2013) DNS at $Re_\tau = 720$; + Singh et al. (2018) DNS at $Re_\tau \approx 640$; \circ den Toonder et al. (1997), measurements at $Re_\tau \approx 630$.

3.2 Multiphase Flow Validation

To validate the coupled DNS and LPT solver, a separate simulation was performed, at $Re_\tau = 277$, and compared directly with the DNS results of Vreman [23] who considered the dispersion of glass beads in a turbulent pipe flow. In the present work, the particles were injected at random locations within the computational domain, initializing their velocities to their interpolated fluid velocity at their location at the start of the particle simulation. 29 400 particles were injected each having a diameter of $60 \mu\text{m}$. To best duplicate the parameters used in the validation case considered [23], only drag and gravitational forces were used when calculating the particle trajectories, with the impact of lift considered negligible. The gravitational force was also applied in the mean flow direction, in line with the validation case conditions. The only difference was that in the present simulation a much larger number of numerical grid nodes were used. One-way and four-way coupled simulations with the same particle size and number were performed, with mean and fluctuating velocity profiles analyzed.

The particle mean velocity profile and stresses are compared with the results of Vreman [23] in Fig. 2. Clearly the present one-way coupled simulations are significantly different from those using four-way coupling, with the latter required to simulate the impact of particles on the continuous phase flow field. There is reasonable agreement between the four-way DNS predictions of Vreman [23] and the present four-way results, although some differences do occur within the bulk flow region, this likely being due to the significantly increased numerical resolution used in the present work (18.7M nodes as opposed to 607k in [23]). One-way coupled results are also included in Fig. 2 to demonstrate the impact of the four-way coupled simulation relative to the system without collisions or particle-fluid interaction.

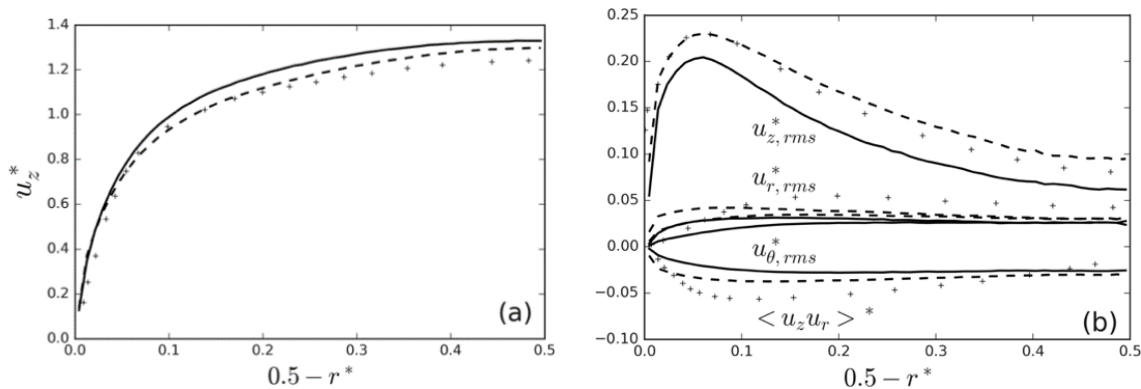


Figure 2. (a) Mean axial velocity and (b) normal and shear stresses at $Re_\tau = 277$: — present DNS one-way coupled; --- present DNS four-way coupled; + Vreman (2007) DNS four-way coupled.

3.3 Particle Deposition

The fully developed $Re_\tau = 720$ flow was used to simulate one- and four-way coupled flows at two different particle Stokes numbers of $St^+ = 5.55$ and 16.78 . In both cases, the same particle volume fraction was used, $\phi = 7 \times 10^{-4}$. To initialize the simulations, 105k particles were randomly injected throughout the computational domain and assigned the local interpolated fluid velocity. The particle parameters were a diameter of $50 \mu\text{m}$ with a density ratio of 7.71 for both Stokes numbers.

Fig. 3 shows the mean streamwise velocity profile and the effects of the non-dimensionalized pressure gradient reduction with time, with the latter used to drive the reduction in mass flow through the pipe in order to reduce the effects of flow velocity and turbulence on suspending the particles and to encourage particle deposition.

Fig. 4 depicts instantaneous fluid velocity contours in the streamwise direction, as pseudo-color contour plots, at different times. These reveal the detailed representation of the turbulent velocity field present in the pipe flow. The highest velocities tend to occur near the center of the pipe in the streamwise direction and show a strong positive motion which weakens over time.

Fig. 5 shows the dispersion function, defined in Eq. (5), and the mean vertical position of the particles with time. At the

high Stokes number, $St^+ = 16.78$, the particle dispersion and their mean vertical position decrease considerably faster with time than for the lower Stokes number case. This is due to the increased gravitational force causing the particles to accelerate in the negative vertical direction at an increased rate. For the particles of $St^+ = 5.55$, the rate of migration towards the lower half of the pipe is much slower when compared to the $St^+ = 16.78$ case.

Fig. 6 presents mean particle concentration profiles in the vertical direction for both particles cases at various points in time, with the concentration normalized by the initially injected concentration, C_0 . The particles are seen to migrate towards the lower wall region and to ultimately deposit on the bottom of the pipe, with the near-wall concentration of the $St^+ = 16.78$ particles higher than for the lower Stokes number case.

This can be seen more clearly in Figs. 7 and 8, which plot the positions of particles in the vertical direction, y^* , and close to the wall ($0.49 \leq r^* \leq 0.5$) in the lower half of the pipe in the circumferential direction x^* with time. Initially, the particles are relatively evenly distributed within the computational domain, but with increasing time migration to the lower regions of the pipe occurs and for the high Stokes number case by $t^* = 50$ a particle bed appears to have formed. In contrast, for the lower Stokes number case a bed is not formed, although

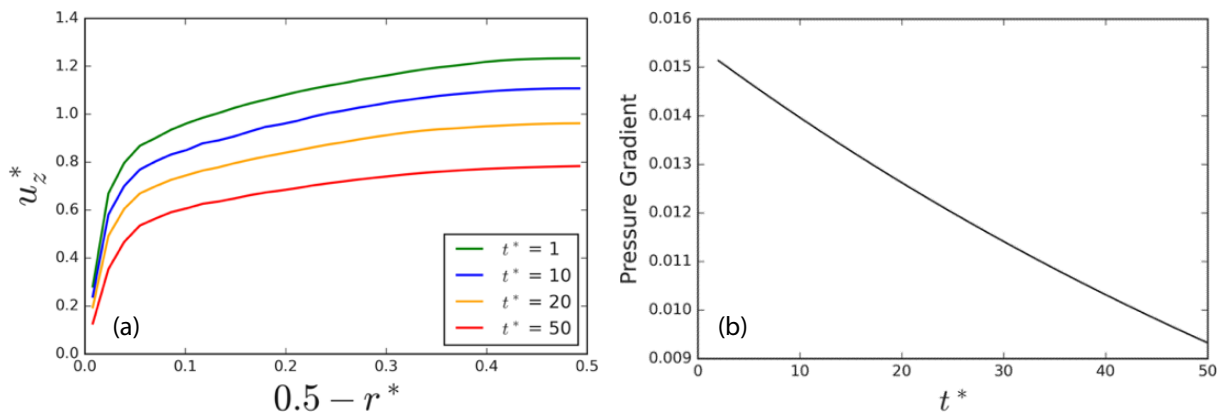


Figure 3. (a) Mean axial velocity at different t^* and (b) prescribed non-dimensional pressure gradient.

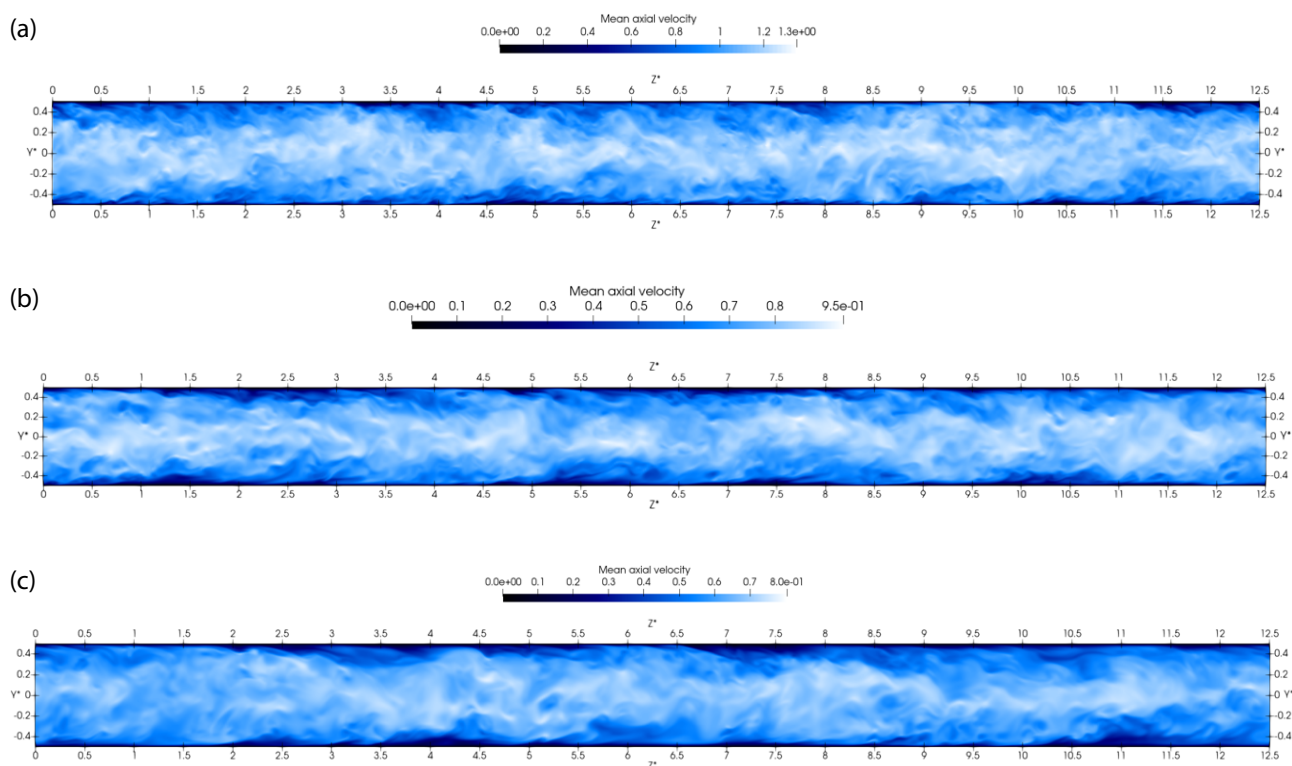


Figure 4. Pseudo-color visualization of the instantaneous axial velocity normalized by the bulk velocity, U_b , at different times. (a) $t^* = 1$, (b) $t^* = 20$, (c) $t^* = 50$.

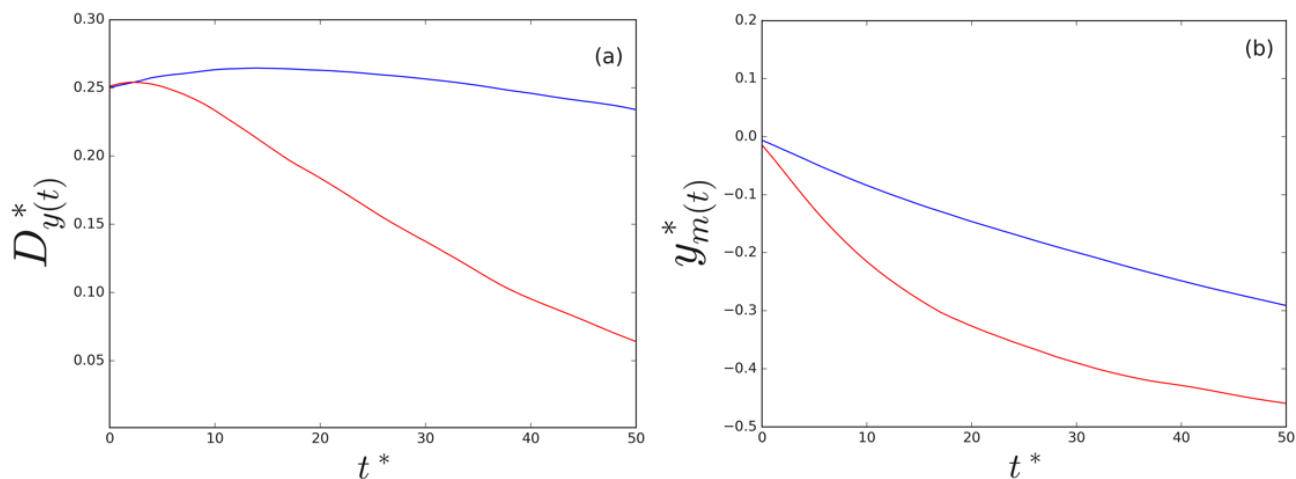


Figure 5. (a) Dispersion function in vertical direction and (b) mean vertical position of particles. Blue: $St^+ = 5.55$; red: $St^+ = 16.78$.

the majority of the particles have migrated towards the bottom of the pipe and formed dune-like structures. These observations are in line with the calculated dispersion function and mean particle position values given in Fig. 5, where from approximately $t^* = 5$ the higher Stokes number particles start to deviate from the lower Stokes number case, and as time increases particle deposition proceeds at a significantly higher rate.

To further examine the local behavior of the particles, probability density functions (PDFs) of particle properties were also

gathered. Fig. 9 shows PDFs for both Stokes number particles for the particle velocity in the vertical direction which illustrates a larger spread of negative vertical velocities for the low Stokes particles. There also exists a slight skew towards negative velocities in both cases due to the influence of gravity. Secondly, PDFs of the particles' streamwise velocity are given, where for the low Stokes number particles two regimes are observed, with some particles possessing low speeds (those trapped in the wall region) or higher speeds (those in the bulk of the flow). The high Stokes number particles do not exhibit

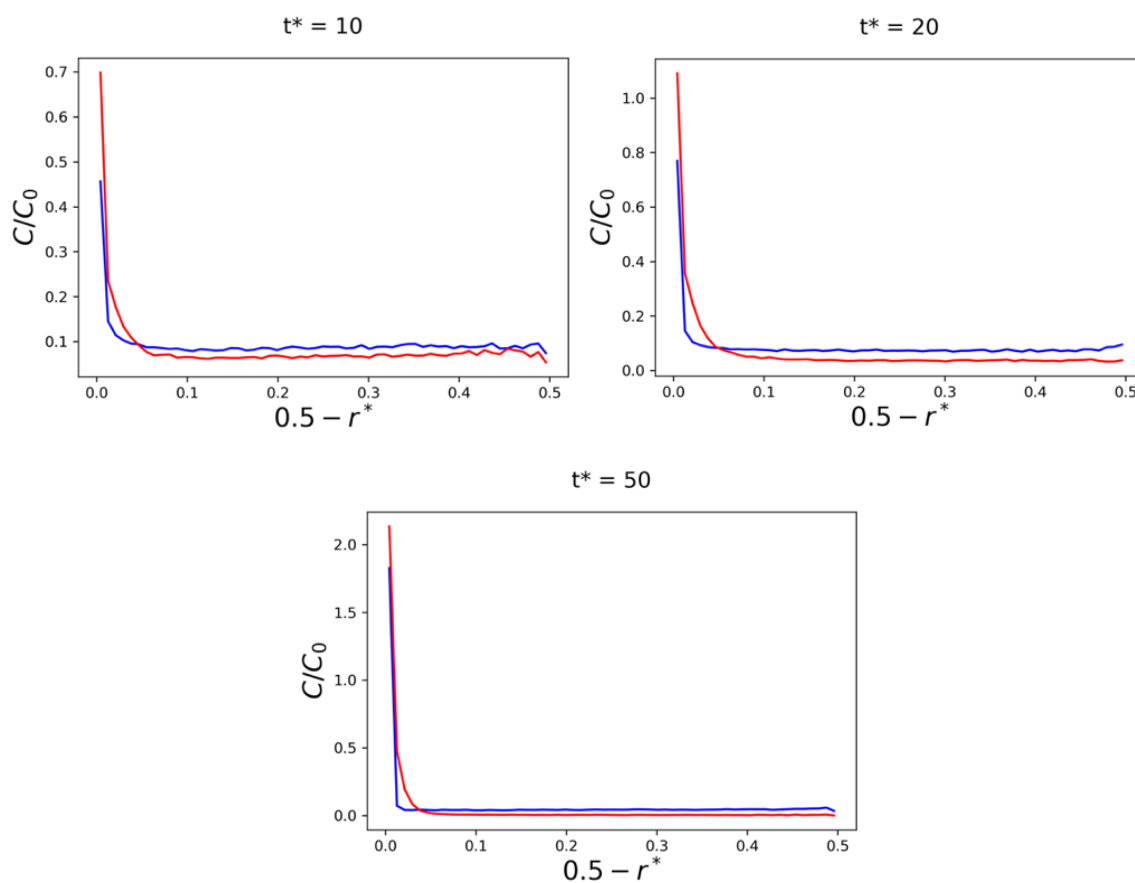


Figure 6. Mean particle concentration of $St^+ = 5.55$ (blue) and $St^+ = 16.78$ (red) particles with time, normalized by initial concentration.

this behavior, with the majority of particles existing at low velocities due to their proximity to the lower wall of the pipe, underlining the importance of flow and particle interactions within the wall region such as particle preferential concentration in low speed streaks (seen in Figs. 7 and 8), and particle interaction with near-wall turbulence structures which, through sweep and ejection events, modulate the particle flux towards the wall.

Particle-turbulence interaction plays an important role in particle migration towards the wall. Turbophoresis and increased gravitational force are expected to cause high Stokes number particles to deposit earlier than lower ones, however, the dependence of critical deposition velocity on Stokes number is strong. The critical deposition velocities, determined by monitoring the particle concentrations in the lower region of the pipe until the particles began to form high-concentration regions there were $u^* = 0.4289$ and 0.7573 for $St^+ \approx 5.55$ and 16.78 , respectively. Similar velocities were obtained by Rice [8].

PDFs of the slip velocity are also given in Fig. 9 which tend to increase as the Stokes number rises, as would be expected for the more inertial particles. The PDFs of the vertical position of the particles is also considered, with the high Stokes particles occupying much greater negative positions, in line with previous observations. Lastly, PDFs of the particle velocity in the circumferential direction and the angle between the vertical and circumferential positions were investigated. The circumfer-

ential direction shows a larger spread in velocities for the high Stokes number which suggests greater particle concentrations close to the wall.

4 Conclusions

This study has considered the effect of particle Stokes number on particle deposition within a wall-bounded turbulent pipe flow. Direct numerical simulations have been performed, coupled with Lagrangian particle tracking, for fully developed turbulent flows, with mean velocity, and normal and shear stress, profiles within single-phase flows demonstrating agreement with other simulation results in the literature and experimental data sets. A similar validation for particle-laden flows has also been performed, again with good agreement with alternative simulations found.

The fully developed $Re_\tau = 720$ pipe flow has been used to perform four-way coupled simulations to predict particle deposition. These were carried out at two different Stokes numbers, $St^+ \approx 5.55$ and 16.78 . The pressure gradient along the pipe was decreased time and the gravitational force was applied in the vertical direction. The conveying flow rate then decreased allowing particle deposition to occur.

From the analysis performed, it can be concluded that particle deposition is sensitive to Stokes number, such that increased

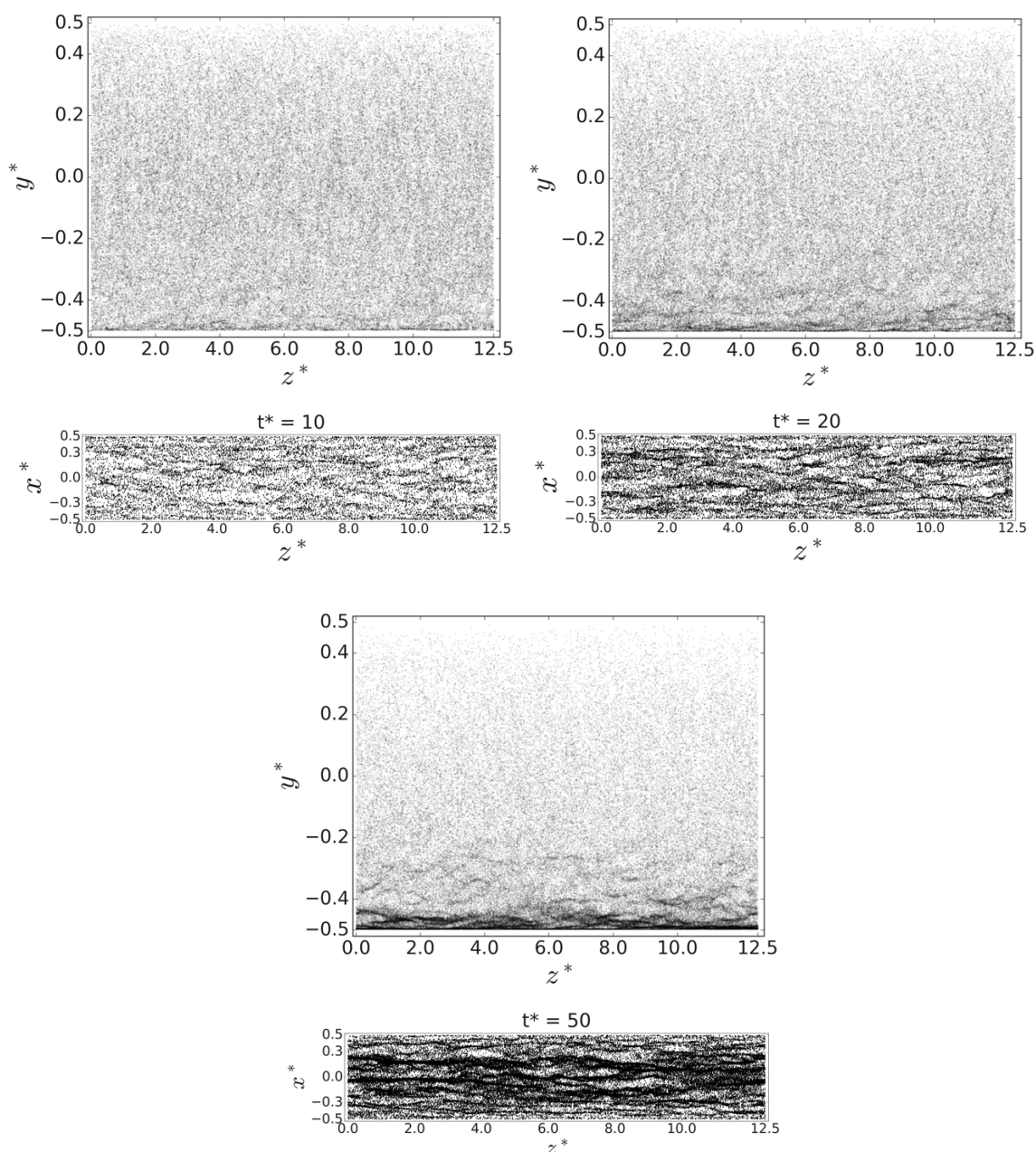


Figure 7. Instantaneous plots of particle position. Top: vertical direction, bottom: near-wall region of the lower half of the pipe for $St^+ \cong 5.55$.

Stokes number particles begin to deposit at higher flow velocities. The determined particle dispersion function and particle mean displacement have been demonstrated to decrease considerably faster with time at higher Stokes numbers due to the increased gravitational force acting on the particles. Particle concentrations demonstrate particle migration towards the lower wall regions and ultimately to deposition on the bottom of the pipe, with a particle bed forming for the higher Stokes number case. In contrast, at lower Stokes number, a bed is not formed, although the majority of the particles do form dune-like structures on the floor of the pipe. Lastly, an analysis of the

particle dynamics, carried out by examining probability density functions of particle velocities and positions, confirmed the above findings, suggesting that in general high Stokes number particles have a greater tendency to form particle beds.

Further work will examine a wider range of particle Stokes numbers and compare critical particle deposition velocities derived from the simulations with those obtained experimentally from both particle deposition and resuspension approaches to determining this parameter.

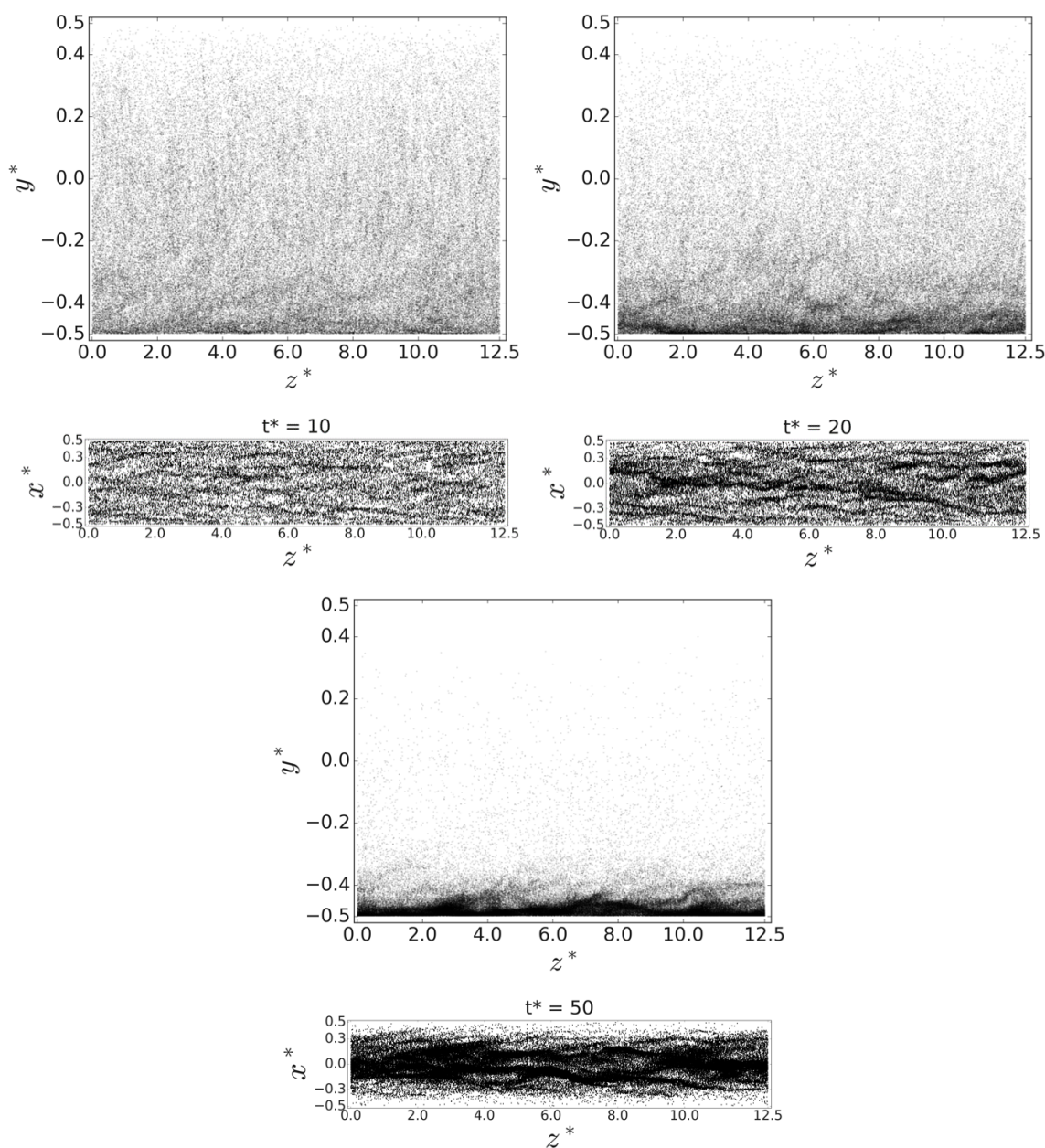


Figure 8. Instantaneous plots of particle position with time. Top: vertical direction, bottom: near-wall region of the lower half of the pipe, for $St^+ \cong 16.78$.

Acknowledgment

The authors are grateful for funding from the UK Engineering and Physical Sciences Research Council and the University of Leeds through the TRANSCEND (Transformative Science and Engineering for Nuclear Decommissioning) project (EP/S01019X/1).

The authors have declared no conflict of interest.

Symbols used

d_p^*	[-]	particle diameter
D	[m]	pipe inner diameter
$D_{y(t)}^*$	[-]	dispersion function
f_i	[-]	flow forcing term
Fr	[-]	Froude number
g	[m s ⁻²]	acceleration due to gravity
\hat{g}	[-]	unit vector in gravity direction
L	[m]	characteristic length scale
N_p	[-]	number of particles

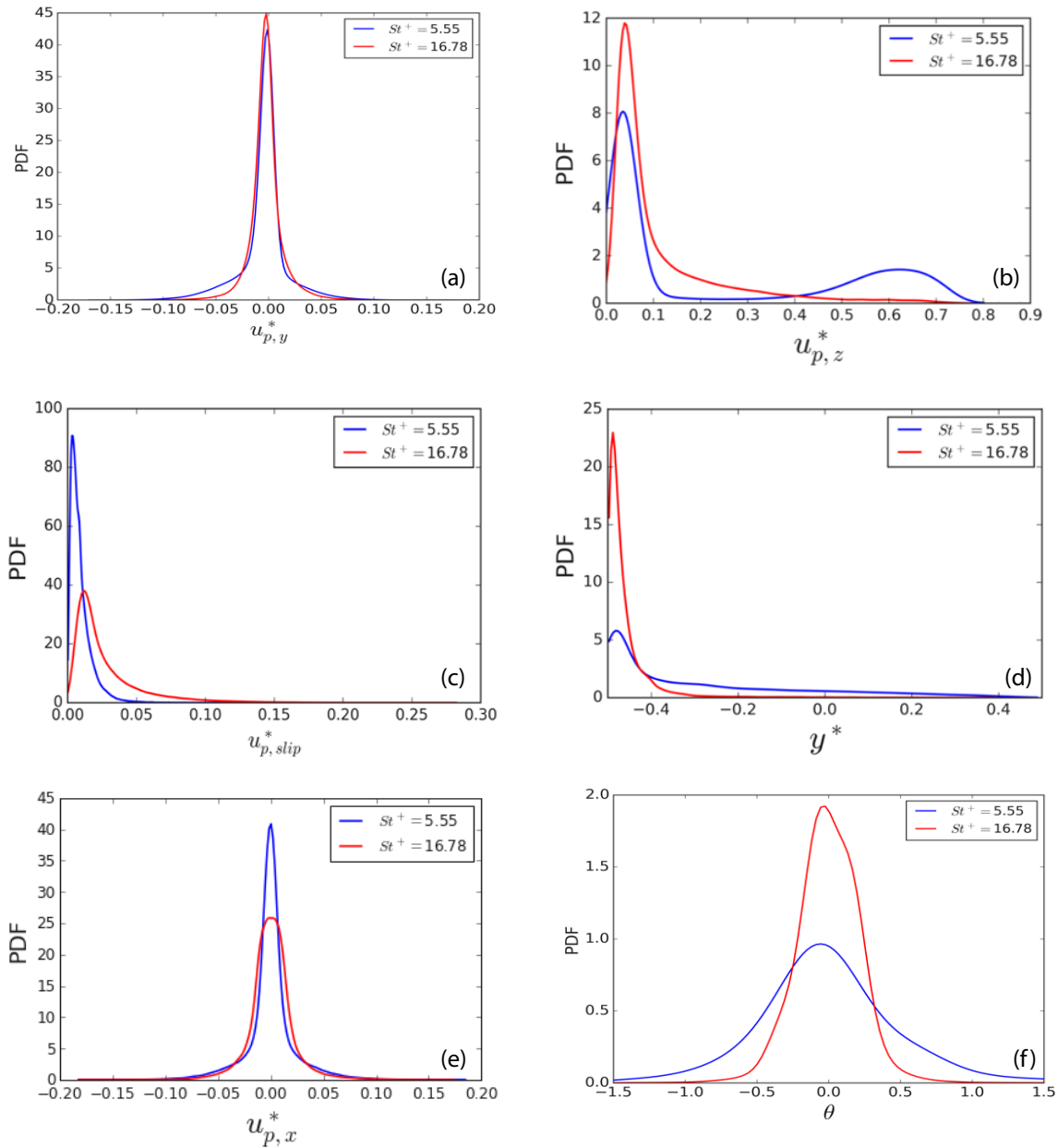


Figure 9. Probability density functions for $St^+ \cong 5.55$ and 16.78 particles at $t^* = 50$: (a) vertical velocity; (b) streamwise velocity; (c) slip velocity; (d) vertical position, (e) circumferential position, (f) angle between vertical and circumferential positions.

p^*	[-]	pressure in bulk units
r	[m]	radial coordinate
R	[m]	pipe radius
Re_b, Re_τ	[-]	bulk and shear Reynolds number
St	[-]	Stokes number
Δt^*	[-]	particle time step
\underline{u}^*	[-]	mean velocity in bulk units
$\underline{u}_p^*, \underline{u}_f^*$	[-]	particle and fluid velocity vector
\underline{u}_s^*	[-]	slip velocity
\underline{u}_τ	[m s ⁻¹]	shear velocity
U_b	[m s ⁻¹]	bulk mean velocity
\underline{x}_p^*	[-]	particle position vector

$y_{i(t)}^*$	[-]	particle vertical position
$y_{m(t)}^*$	[-]	particle vertical mean position
z	[m]	axial position
Greek letters		
θ	[-]	azimuthal coordinate
μ	[Pa s]	dynamic viscosity
ν	[m ² s ⁻¹]	kinematic viscosity
ρ	[kg m ⁻³]	fluid density
$\rho_f \rho_s$	[kg m ⁻³]	density of fluid and solid phase
ρ_p^*	[-]	particle-fluid density ratio
$\underline{\tau}$	[Pa]	fluid stress tensor

ϕ	[-]	volume fraction
ω_f^*	[-]	vorticity of fluid

Sub- and superscripts

x, y, z	Cartesian coordinates
*	non-dimensional bulk units
+	non-dimensional shear units

Abbreviations

DNS	direct numerical simulation
GLL	Gauss-Lobatto-Legendre
LPT	Lagrangian particle tracking/tracker
PDF	probability density function

References

- [1] D. Guha, P. A. Ramachandran, M. P. Dudukovic, *Chem. Eng. Sci.* **2007**, *62* (22), 6143–6154. DOI: <https://doi.org/10.1016/j.ces.2007.06.033>
- [2] J. M. J. den Toonder, M. A. Hulsen, G. D. C. Kuiken, F. T. M. Nieuwstadt, *J. Fluid Mech.* **1996**, *337*, 193–231. DOI: <https://doi.org/10.1017/S0022112097004850>
- [3] P. Orlandi, M. Fatica, *J. Fluid Mech.* **1997**, *343*, 43–72. DOI: <https://doi.org/10.1017/S0022112097005715>
- [4] C. Wagner, T. J. Hüttl, R. J. Friedrich, *Comp. Fluids* **2001**, *30* (5), 581–590. DOI: [https://doi.org/10.1016/S0045-7930\(01\)00007-X](https://doi.org/10.1016/S0045-7930(01)00007-X)
- [5] K. Fukagata, N. Kasagi, *J. Comput. Phys.* **2002**, *181* (2), 478–498. DOI: <https://doi.org/10.1006/jcph.2002.7138>
- [6] G. S. El Khoury, P. Schlatter, A. Noorani, P. F. Fischer, G. Brethouwer, A. V. Johansson, *Flow Turbul. Combust.* **2013**, *91* (5), 475–495. DOI: <https://doi.org/10.1007/s10494-013-9482-8>
- [7] Y. Tsuji, Y. Morikawa, H. Shiomi, *J. Fluid Mech.* **1984**, *139*, 417–434. DOI: <https://doi.org/10.1017/S0022112084000422>
- [8] H. P. Rice, Transport and deposition behaviour of model slurries in closed pipe flow, *Ph.D. Thesis*, University of Leeds, **2013**.
- [9] P. F. Fischer, J. W. Lottes, S. G. Kerkemeier, Nek5000, **2008**. <http://nek5000.mcs.anl.gov> (Accessed on November 12, 2021)
- [10] A. T. Patera, *J. Comput. Phys.* **1984**, *54* (3), 468–488. DOI: [https://doi.org/10.1016/0021-9991\(84\)90128-1](https://doi.org/10.1016/0021-9991(84)90128-1)
- [11] Y. Maday, A. T. Patera, in *State-of-the-Art Surveys on Computational Mechanics* (Eds: A. K. Noor, J. Tinsley Oden), American Society of Mechanical Engineers, **1989**.
- [12] M. R. Maxey, J. J. Riley, *Phys. Fluids* **1983**, *26* (4), 883–889. DOI: <https://doi.org/10.1063/1.864230>
- [13] L. F. Mortimer, D. O. Njobuenwu, M. Fairweather, *Phys. Fluids* **2019**, *31* (6), 063302. DOI: <https://doi.org/10.1063/1.5093391>
- [14] L. Schiller, Neue quantitative Versuche zur Turbulenzentstehung, *Z. Angew. Math. Mech.* **1934**, *14* (1), 36–42. DOI: <https://doi.org/10.1002/zamm.19340140105>
- [15] P. Saffman, *J. Fluid Mech.* **1965**, *22* (2), 385–400. DOI: <https://doi.org/10.1017/S0022112065000824>
- [16] D. S. Dandy, H. A. Dwyer, *J. Fluid Mech.* **1990**, *216*, 381–410. DOI: <https://doi.org/10.1017/S0022112090000477>
- [17] G. G. Stokes, *Trans. Cambridge Philos. Soc.* **1851**, *9*, 8–106.
- [18] L. F. Mortimer, D. O. Njobuenwu, M. Fairweather, *Phys. Fluids* **2020**, *32* (4), 043301. DOI: <https://doi.org/10.1063/5.0001596>
- [19] C. G. Sinclair, The limit deposit-velocity of heterogeneous suspensions. Symposium on the Interaction between Fluids and Particles, *Third Congress of the European Federation of Chemical Engineers*, London **1962**.
- [20] S. Al-lababidi, W. Yan, H. Yeung, *J. Energy Resour. Technol.* **2012**, *134* (3), 034501. DOI: <https://doi.org/10.1115/1.4006433>
- [21] M. Fairweather, J. Yao, *AIChE J.* **2009**, *55* (7), 1667–1679. DOI: <https://doi.org/10.1002/aic.11798>
- [22] J. Singh, M. Rudman, H. M. Blackburn, *Phys. Rev. Fluids* **2018**, *3* (9), 094607. DOI: <https://doi.org/10.1103/PhysRevFluids.3.094607>
- [23] A. W. Vreman, *J. Fluid Mech.* **2007**, *584*, 235–279. DOI: <https://doi.org/10.1017/S0022112007006556>